ACCSCIENCE PUBLISHING

International Journal of Bioprinting

RESEARCH ARTICLE

Synergistic bone regeneration by surface-modified 3D-printed PCL/β-TCP scaffolds in various animal defect models

Yulin Jiang[1], Guanghui Xi[1], Chen Zhou[1], Haisong Xu[3]*, Xi Yang[1]*, and Dongxu Ke[1,2]*

[1]Novaprint Therapeutics Suzhou Co., Ltd., Suzhou, Jiangsu, China

[2]Department of Biomedical Engineering, Nanjing University Suzhou Campus, Suzhou, Jiangsu, China

[3]Department of Plastic and Reconstructive Surgery, Shanghai Ninth People's Hospital, School of Medicine, Shanghai Jiao Tong University, Shanghai, China

(This article belongs to the *Special Issue*: *Future Bioprinting—Celebrating the 10th Anniversary of the International Journal of Bioprinting*)

Abstract

The regeneration of large-segmental bone defects remains a significant clinical challenge due to their complex microenvironments. Three-dimensional (3D)-printed polycaprolactone (PCL) scaffolds offer a potential solution but exhibit limited osteoinductive capacity. In this study, 3D-printed PCL/β-tricalcium phosphate (TCP) composite scaffolds were pretreated with NaOH, followed by functionalization with bioactive collagen and β-TCP. These modifications markedly improved the scaffolds' hydrophilicity without compromising mechanical integrity. *In vitro* studies with MC3T3-E1 cells demonstrated that the CS@TCP scaffolds significantly enhanced early osteogenic differentiation compared to C, CS, and CS@COL scaffolds, as indicated by the alkaline phosphatase activity assay. *In vivo* evaluation using three different rabbit cranial defect models revealed superior new bone formation in the partial-thickness cranial defect (PTD) groups compared to the full-thickness cranial defect (FTD) and intact cranial bone onlay (Onlay) groups, potentially due to the increased vascularization and abundant endogenous stem cells in the PTD groups. Despite reduced new bone formation in the Onlay group, its bone integration advantages may be advantageous for cosmetic surgery applications. This study investigated how β-TCP surface modification interacts with clinical application-specific microenvironments to maximize the regenerative potential of 3D-printed scaffolds, providing crucial guidance for scaffold design in effective bone defect repair across various clinical scenarios.

Keywords: 3D-printed scaffolds; *In vitro* proliferation and differentiation; Multiple animal defect models; Surface modification

***Corresponding authors:**
Haisong Xu
(113056@sh9hospital.org.cn)

Xi Yang
(Kathy.Yang@3dnovaprint.com)

Dongxu Ke
(dongxu.ke@wsu.edu)

Citation: Jiang Y, Xi G, Zhou C, Xu H, Yang X, Ke D. Synergistic bone regeneration by surface-modified 3D-printed PCL/β-TCP scaffolds in various animal defect models. *Int J Bioprint*. 2025;11(6):390-406. doi: 10.36922/IJB025380386

Received: September 17, 2025
Revised: October 25, 2025
Accepted: November 3, 2025
Published Online: November 3, 2025

1. Introduction

Effective treatment of large-segmental bone defects represents a globally unmet medical need. In the United States (US) alone, approximately 500,000 patients require

surgical intervention for non-healing bone defects annually, while developing countries face higher burdens due to limited access to advanced treatments.[1] Current gold-standard therapies, autografts and allografts, are constrained by donor site morbidity, limited availability, and immunological rejection risks. The economic burden is substantial, with annual healthcare costs exceeding USD 12 billion in the United States for complications related to failed bone defect repairs, emphasizing the urgent need for tissue-engineered solutions capable of addressing this pervasive clinical challenge.[2]

Bone tissue engineering has emerged as a promising alternative for bone defect repair, integrating principles from developmental biology, biomechanics, and materials science to fabricate biomimetic scaffolds that recapitulate the structural hierarchy and functional complexity of native bone tissue.[3,4] Recently, the advent of three-dimensional (3D) printing technologies has revolutionized scaffold fabrication in bone tissue engineering by enabling precise architectural control across multiple length scales.[5] Macroscale optimization of 3D-printed constructs ensures mechanical integrity to withstand physiological loading while maintaining interconnected porosity for new bone ingrowth.[6–8] In addition, microscale modification of 3D-printed scaffolds facilitates cellular attachment, proliferation, and differentiation, promoting new bone formation.

With this powerful tool, many studies have reported 3D-printed biodegradable scaffolds for bone tissue engineering applications. For example, Wang *et al.*[9] developed a hierarchical polycaprolactone (PCL)/β-tricalcium phosphate (TCP) scaffold combining fused deposition modeling (FDM) printed macrofibers and melt electrowriting (MEW) printed microfibers to promote cell infiltration and osteogenesis. While effective, they focused primarily on scaffold structure and composition, without further investigating the regenerative potential of functionalized scaffolds. In another work, Weingärtner *et al.*[10] fabricated 3D-printed PCL scaffolds followed by coating with type I collagen. The biocompatibility of the scaffolds was evaluated by culturing three different cell types on them. Results showed that the collagen coating significantly improved the cell–scaffold interaction. However, their work was primarily focused on *in vitro* cellular responses, without evaluating the performance of the functionalized scaffolds *in vivo*. Taken together, few studies have evaluated the combined effects of the functionalized scaffolds in different clinically relevant bone defect models.

In this study, 3D-printed PCL/β-TCP scaffolds with surface functionalization were constructed to improve osteogenic performance. The surface modification was facilitated using NaOH immersion, followed by collagen coating through vacuum-assisted adsorption, and β-TCP coating by dip-coating deposition. Chemical, physical, and mechanical characterizations confirmed the successful fabrication of bioactive composite scaffolds. Furthermore, the biological performance of the 3D-printed scaffolds was assessed *in vitro* using 3-(4,5-dimethylthiazol-2-yl)-2,5-diphenyltetrazolium bromide (MTT) assay, live/dead staining, alkaline phosphatase (ALP) activity, and alizarin red S (ARS) staining. The results showed that the modified scaffolds significantly promoted cell proliferation and osteogenic differentiation. Finally, the 3D-printed scaffolds were implanted in rabbits' full-thickness cranial defects (FTD), partial-thickness cranial defects (PTD), and onlay placement on intact cranial bone (Onlay), followed by micro-computed tomography (CT), histological, and immunohistochemical analysis to assess *in vivo* osteogenesis and angiogenesis. The implantation demonstrated enhanced new bone formation and angiogenesis in the PTD group. Collectively, this study aims to develop and systematically evaluate multifunctional 3D-printed scaffolds that integrate bioactivity and osteogenic potential, providing comprehensive insights into their translational applicability for effective bone defect repair across diverse clinical scenarios.

2. Materials and methods

2.1. Materials

Polycaprolactone was acquired from Evonik (China), β-TCP powder from DinganTec (China), and collagen from Trauer (China). MC3T3-E1 subclone 14 (CL-0378), basal medium, osteogenic differentiation medium, and ARS solution were supplied by Wuhan Pricella Biotechnology Co., Ltd (China). MTT, live/dead staining kits, ALP assay kits, and 5-bromo-4-chloro-3-indolyl phosphate (BCIP)/nitro blue tetrazolium (NBT) alkaline phosphatase color development kits were provided by Beyotime (China). Hematoxylin and eosin (H&E) staining kits, Goldner's trichrome staining kits, Masson's trichrome staining kits, phosphate-buffered saline (PBS), and paraformaldehyde (PFA) were obtained from Solarbio (China). The primary anti-collagen I (COL) and anti-von Willebrand factor (vWF) antibodies were purchased from Absin (China). All other reagents were purchased from Sigma-Aldrich (USA).

2.2. Scaffold design

A regular triangular pore architecture with a filament diameter of 200 μm and a pore size of 600 μm was selected for the scaffold design based on previous studies.[11] Cuboid scaffolds with dimensions of $4 \times 4 \times 1$ mm^3 were fabricated for cell assays, while larger ones ($5.4 \times 10 \times 10$ mm^3) were used for compressive strength testing. For the animal study, circular plug samples with (dimensions diameter × diameter × height × height) of 15 mm × 10 mm × 1.5 mm

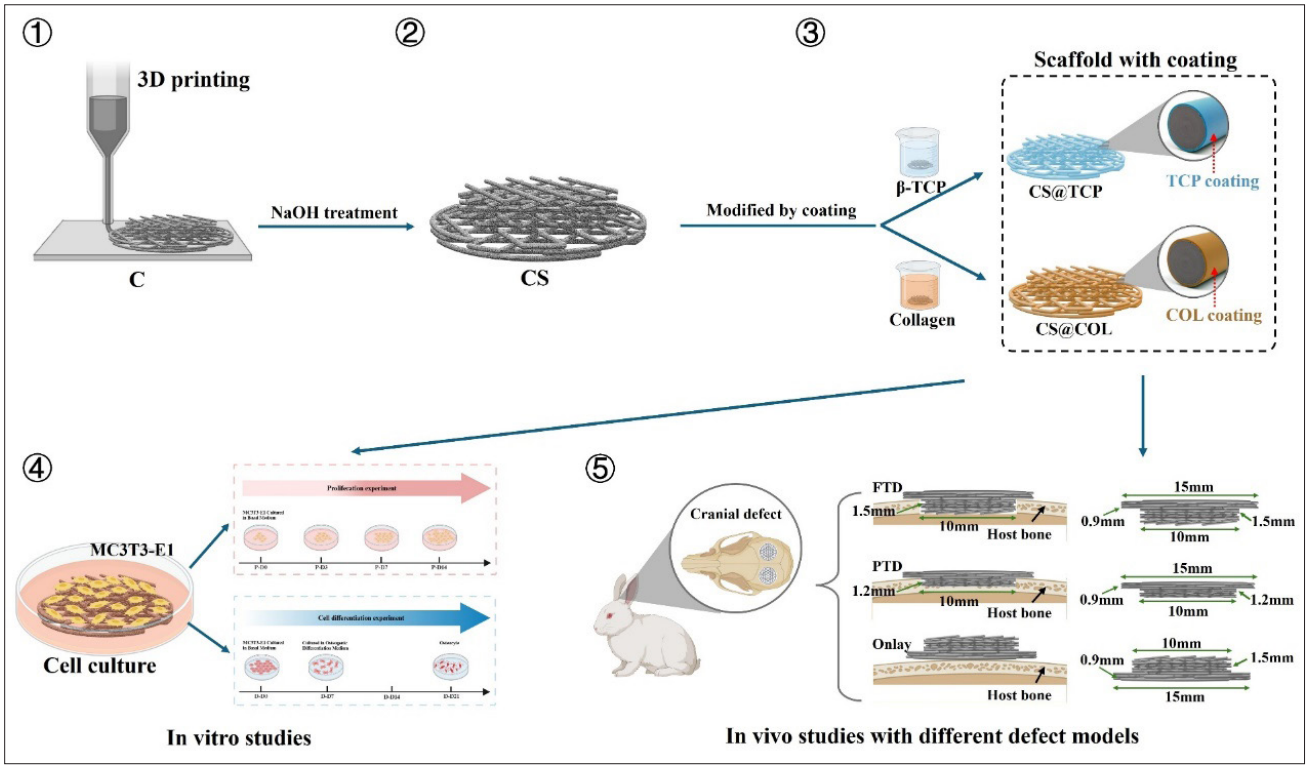

Figure 1. Schematic illustration of the research process of this study. Abbreviations: β-TCP, beta-tricalcium phosphate; C, polycaprolactone/β-tricalcium phosphate; COL, collagen; CS, NaOH-treated polycaprolactone/β-tricalcium phosphate; FTD, full-thickness cranial defect; Onlay, intact cranial bone as an onlay graft; PTD, partial-thickness cranial defect.

× 0.9 mm (FTD), 15 mm × 10 mm × 1.2 mm × 0.9 mm (PTD), and 15 mm × 10 mm × 1.5 mm × 0.9 mm (Onlay) were prepared for different defect models.

2.3. Fabrication of 3D-printed scaffolds

According to the previous study, PCL was added to dichloromethane and mixed at 500 rpm until it was fully dissolved.[12] Then, β-TCP was added to reach a concentration of 20 wt.%. After mixing for 4 h, the solution was poured onto a stainless-steel plate. The dichloromethane was evaporated at 37°C for 24 h, forming thin PCL/β-TCP films. Finally, the films were cut into 5 × 5 mm^2 pieces for printing.

The 3D-printed scaffolds were fabricated using a melt-extrusion-based additive manufacturing system, Organ Printing United System (OPUS, Novaprint Therapeutics, China). The printing parameters were as follows: the syringe temperature was set to 120°C, the extrusion pressure to 750 kPa, the printing speed to 220 mm/min, and the layer thickness to 0.1 mm. Scaffolds were fabricated using tapered steel nozzles with a 200-μm inner diameter, while the printing platform was maintained at 37°C. The printed scaffolds without NaOH treatment were designated as C in the present study.

2.4. Surface modification

The scaffolds were first immersed in 2 mol/L NaOH solution and incubated on a shaker at 37°C for 24 h. After incubation, the solution was removed, and the scaffolds were washed in distilled water using ultrasonication for 5 min. Finally, the scaffolds were dried overnight at 37°C and divided into the following three groups (Figure 1):

- CS group: NaOH-treated and dried scaffolds.
- CS@COL group: NaOH-treated scaffolds immersed in an 8 mg/mL collagen solution and subjected to a 30-min vacuum pressure impregnation, followed by incubation on a shaker at 37°C for 24 h and drying on a Teflon plate at 45°C for 24 h.
- CS@TCP group: NaOH-treated scaffolds immersed in a 1 mg/mL β-TCP suspension and stirred at 500 rpm for 24 h. After treatment, the scaffolds were rinsed three times with distilled water for 5 min each and dried overnight at 37°C.

2.5. Physical, chemical, and mechanical characterizations

The morphology of the scaffolds was observed using scanning electron microscopy (SEM) (S8100, Hitachi,

Japan). The scaffolds were coated with platinum for 180 s and then observed at an accelerating voltage of 3.0 kV. Meanwhile, elemental analyses of the scaffolds were performed using energy dispersive X-ray spectroscopy (EDS).

Next, Fourier transform infrared spectroscopy (FTIR) analysis was conducted to identify the functional groups in the scaffolds. This experiment was performed using an FTIR spectrometer (iS50, Thermo Fisher Scientific, USA) with a wavelength of 4000–400 cm^{-1}.

Optical contact angles were measured using an OCA 15EC goniometer (DataPhysics Instruments, Filderstadt, Germany). A 3 μL deionized water droplet was deposited on the sample surface using a microsyringe. Images of the droplets were captured through a high-resolution camera (EOS 5D, Canon, Japan), and contact angles were analyzed using Surface contact angle (SCA) software (DataPhysics Instruments, Filderstadt, Germany).

The compressive properties of the scaffolds were determined by a compression test using a universal testing system (HY-1080, Shanghai Heng Wing Precision Instrument, China) with a 1000 N load cell. Scaffold samples with dimensions of 5.4 × 10 × 10 mm^3 were compressed at a constant crosshead speed of 5 mm/min, while compressive strengths and compressive modulus were calculated (n = 4).

2.6. Cell proliferation

After ethylene oxide sterilization, four scaffold groups (C, CS, CS@COL, and CS@TCP) were placed into 96-well plates. MC3T3-E1 cells were seeded onto the scaffolds at a density of 1 × 10^5 cells per well and incubated at 37 °C with 5% CO_2 for 3, 7, and 14 days, as illustrated in Figure 4A. The medium was changed every 3 days.

2.7. MTT assay

The samples were treated with 10 μL of 5 mg/mL MTT solution (medium:MTT = 10:1) and incubated at 37°C for 4 h in the dark. After incubation, the supernatant was carefully removed from the wells. Then, 700 μL of dimethyl sulfoxide was added to the samples and shaken on a micro-oscillator for 30 min to ensure complete dissolution. After dissolution, 100 μL of supernatant was transferred into a 96-well plate and the absorbance was measured at 570 nm using a microplate reader (SpectraMax i3x, Molecular device, USA).

2.8. Stability analysis of different coatings

Samples were collected after 0 and 14 days of cell proliferation incubation, followed by fixation in 4% glutaraldehyde for 24 h. Then, the samples were dehydrated through a graded ethanol series (30%, 50%, 70%, 80%, 90%, 95%, and 100%) for 10 min at each step and dried. Finally, the dried samples were coated with platinum for 180 s and then observed at an accelerating voltage of 3.0 kV. Meanwhile, the elemental analyses of the scaffolds were performed using EDS.

2.9. Cell differentiation

MC3T3-E1 cells were seeded onto sterilized scaffolds (C, CS, CS@COL, and CS@TCP) at a density of 1 × 10^5 cells per well. The basic medium was applied for 7 days and then replaced with an osteogenic induction medium for 14 days, as shown in Figure 5A. The osteogenic induction medium was refreshed every 2–3 days.

2.10. Live/dead staining

Cell viability was evaluated using a live-dead staining working solution, which was prepared by mixing calcein acetoxymethyl ester and propidium iodide solutions at a 1:1 ratio. After culture, the culture medium was discarded, and the scaffolds were washed three times with PBS. Following the manufacturer's protocol, 100 μL of the working solution was applied to each well and incubated at 37 °C for 30 min in the dark. Post-incubation, the solution was removed, followed by three washes in PBS. Finally, fluorescent images were captured using an inverted fluorescence microscope (Ts2-FL, Nikon, Japan).

2.11. Alkaline phosphatase staining and activity

At Days 14 and 21 of osteogenic differentiation culture, BCIP/NBT staining was performed to visualize ALP activity. The working solution was prepared by dissolving 10 μL of BCIP and 20 μL of NBT in 3 mL of PBS. A total of 100 μL of the prepared working solution was added to each well and incubated at room temperature for 30 min in the dark. Following incubation, images were acquired using a light microscope (DMi1, Leica, Germany).

Meanwhile, ALP activity was quantitatively analyzed using an enzymatic assay. The scaffolds were lysed with a cell lysis solution and incubated on ice for 10 min. The lysate was collected, and 50 μL of the cell lysate was combined with 50 μL of a chromogenic substrate solution. The reaction was initiated by incubating the mixture at 37 °C for 30 min. To terminate the reaction, 100 μL of a stopping solution was added. The absorbance at 570 nm was measured using the SpectraMax i3x microplate reader. The concentration of *p*-nitrophenol generated was calculated based on the standard curve.

2.12. Alizarin red S staining and quantification

Samples were washed three times with PBS, followed by fixation with 4% PFA for 1 h on Days 14 and 21 of osteogenic differentiation culture. Subsequently, 100 μL of ARS working solution was added to each well,

followed by incubation at room temperature for 30 min in the dark. Afterward, samples were washed gently with deionized water, and images were captured using the DMi1microscope a light microscope. Additionally, 200 µL of 10% cetylpyridinium chloride solution was added to each well, followed by incubation on a shaker at 37°C for 30 min in the dark. Subsequently, 100 µL of the resulting mixture was transferred into a 96-well plate, and the absorbance was measured at 570 nm using the SpectraMax i3x microplate reader.

2.13. *In vivo* studies using different rabbit cranial defect models

In this study, 12 male New Zealand white rabbits aged 6 months were used. Two individual cranial defects were induced in each rabbit, and the defects were divided into the following three different groups (n = 4): FTD, PTD, and Onlay groups, as shown in **Table 1**. Prior to surgery, scaffolds and surgical equipment were sterilized with ethylene oxide, and rabbits were anesthetized with a gaseous mixture of oxygen and isoflurane. After the surgical area was shaved, sanitized, and incised, FTD and 1.2 mm PTD were created by a trephine or surgical drill. Then, the scaffolds were implanted and secured with screws at the defect sites, followed by wound closure by suturing. Additionally, in the Onlay group, the scaffolds were placed on top of the rabbits' intact cranial bone as a graft, as shown in Figure 1. After 12 and 26 weeks, animals were euthanized by carbon dioxide inhalation. The harvested samples were fixed in 10% neutral buffered formalin for at least 3 days before further analysis.

2.14. Micro-computed tomography analysis

A high-resolution micro-CT scanner (Skyscan 1172, Skyscan, Belgium) was used to analyze the new bone formation. Scanning was performed with a voxel size of 20 µm, an X-ray voltage of 80 kV, an electric current of 112 µA, and a rotation step of 0.6°. After scanning, images were reconstructed using the Mimics software (Mimics 21.0, Materialise NV, Belgium). A cylindrical volume of interest with a 10-mm diameter and 1.5-mm height around the defect area was selected for qualitative and quantitative analyses. Bone volume/total volume fraction (BV/TV), trabecular thickness (Tb.Th), bone mineral density (BMD), and trabecular number (Tb.N) were measured for different defect models after implantation for 12 and 26 weeks.

2.15. Histological analysis

Samples were first fixed in 4% PFA for at least 3 days, followed by decalcification in 15% ethylenediaminetetraacetic acid (EDTA) and dehydration through a graded ethanol series. After dehydration, the specimens were embedded in paraffin and sectioned into 5-µm-thick slices using a microtome (RM2016, Leica, Germany). The sections were mounted on glass slides, deparaffinized with xylene, and rehydrated through a descending ethanol series. Subsequently, H&E, Goldner's trichrome, and Masson's trichrome staining were carried out. Images were acquired using the OLYMPUS BX51, Olympus Corporation light microscope.

2.16. Immunohistochemical analysis

Samples were first fixed in 4% PFA and decalcified in 15% EDTA. After decalcification, samples were embedded in

Table 1. Experimental design of the *in vivo* study

Time point	Rabbit ID	Implantation site	
		Right	Left
12 weeks	1	FTD	PTD
	2	FTD	Onlay
	3	PTD	Onlay
	4	PTD	FTD
	5	Onlay	PTD
	6	Onlay	FTD
26 weeks	7	FTD	PTD
	8	FTD	Onlay
	9	PTD	Onlay
	10	PTD	FTD
	11	Onlay	PTD
	12	Onlay	FTD

Abbreviations: FTD, full-thickness cranial defect; Onlay, intact cranial bone as an onlay graft; PTD, partial-thickness cranial defect.

paraffin, followed by sectioning into 5-μm-thick slices using the RM2016 microtome.

Sections were deparaffinized in xylene and rehydrated in a series of graded ethanols and water. Then, antigen retrieval was performed in citrate buffer, followed by quenching of endogenous peroxidase activity with peroxidase block solution at room temperature for 20 min. To prevent nonspecific binding of the secondary antibody, sections were incubated in blocking solution (3% BSA and 0.3% Triton ×100 in PBS) at room temperature for 15 min. Subsequently, sections were incubated overnight at 4 °C with primary antibodies against vWF and COL, followed by 30 min incubation with a biotinylated secondary antibody at room temperature. Finally, images were visualized using the OLYMPUS BX51 light microscope.

2.17. Statistical analysis

Quantitative data were collected from at least three independent experiments per group. Data were expressed as mean ± standard deviation (SD), and one-way analysis of variance (ANOVA) was used to analyze differences between groups. A p-value of less than 0.05 was considered statistically significant ($^*p < 0.05$). Statistical significance was determined using Origin software (Origin 2021, OriginLab Corporation, USA)and GraphPad Prism software (GraphPad 9.5, Graphpad Software Inc., USA)

3. Results

3.1. Microstructure, chemical composition, and compressive strength analysis

An interconnected porous structure was observed in the 3D-printed scaffolds. Compared to the smooth surface of the C scaffold, nanoscale pits appeared on the CS scaffold surface. In addition, a collagen film and nanoscale particles were observed on the surfaces of CS@COL and CS@TCP scaffolds, respectively, as shown in Figure 2A.

No significant differences were observed between the C and CS scaffolds. In contrast, the N peak intensity and content were significantly higher in the CS@COL scaffolds than in the CS group. Moreover, strong Ca and P peaks and increased elemental content were observed in CS@TCP scaffolds compared to CS scaffolds, as shown in Figure 2B. Furthermore, the uniform distribution of C and N elements on the CS@COL scaffolds confirmed the even coverage of the collagen coating, while the uniform Ca distribution on the CS@TCP scaffolds demonstrated the well-distributed β-TCP coating, as shown in Figure 2C.

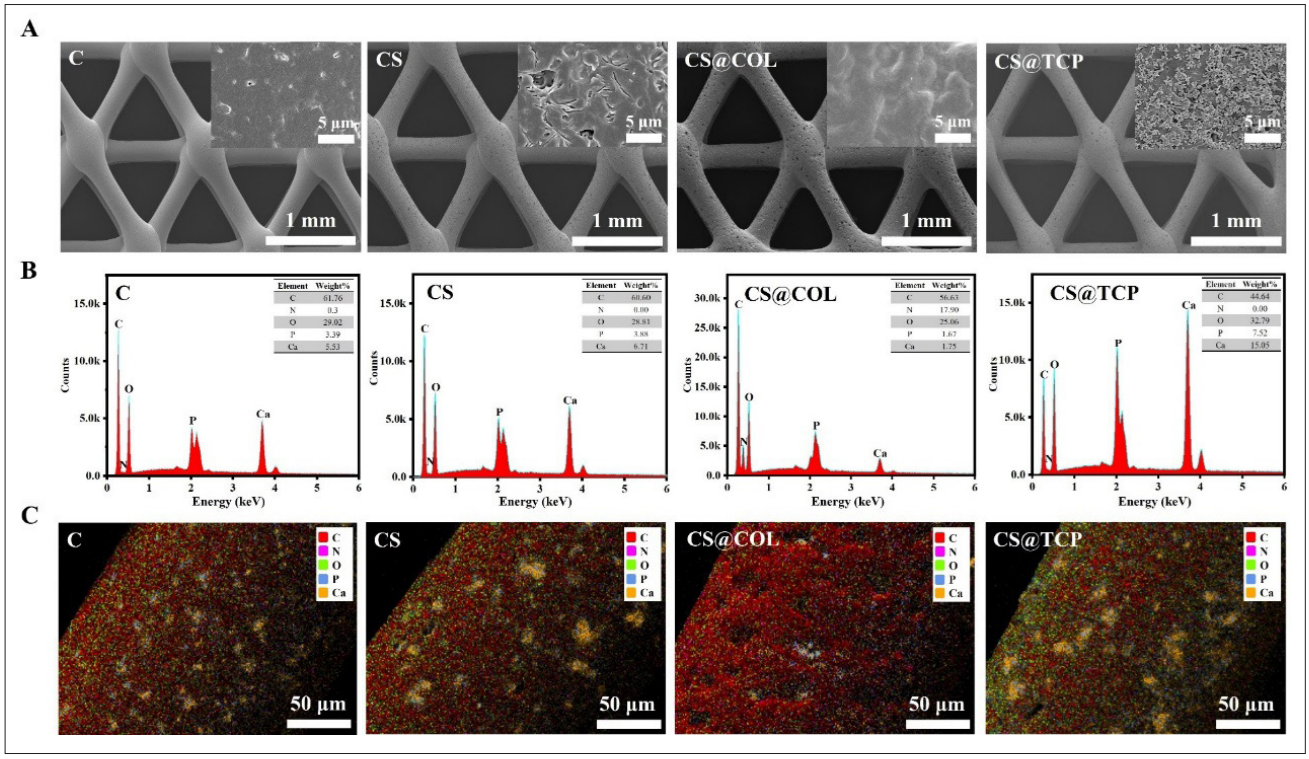

Figure 2. Surface morphology and elemental analysis of different scaffolds. (A) Scanning electron microscopy images. Scale bars: 1 mm, 5 μm (inset); magnifications: ×50, ×10,000 (inset). (B) Energy dispersive X-ray spectroscopy (EDS) spectrum. (C) EDS mapping C, CS, CS@COL, and CS@TCP scaffolds. Scale bars: 50 μm; magnifications: ×500.

The peaks observed at 1720, 2943, and 2864 cm^{-1} in all scaffolds were characteristic bands of PCL, corresponding to the stretching vibration of the carbonyl group (C=O) and the asymmetric stretching vibrations of the CH_2 groups, respectively. Notably, the intensity of the peak at 1043 cm^{-1} significantly increased after the application of β-TCP coating on the CS scaffolds. Additionally, the peaks observed at 3315, 1659, and 1554 cm^{-1} in CS@COL scaffolds corresponded to the amide A (N–H stretching), amide I (C=O stretching), and amide II (N–H bending and C–N stretching) bands, respectively, all of which were typically associated with collagen, as shown in Figure 3A. Furthermore, the contact angles in the C scaffolds were significantly higher than those in the CS, CS@COL, and CS@TCP scaffolds, as presented in Figure 3B. The compressive strength of C (3.48 ± 0.23 MPa) was higher than CS (3.00 ± 0.33 MPa), CS@COL (3.06 ± 0.15 MPa), and CS@TCP (3.10 ± 0.19 MPa) scaffolds; however, no significant differences were observed among them, as presented in Figure 3D. The compressive modulus data showed the same trend, with no significant differences among different groups, as shown in Figure 3E.

3.2. *In vitro* study of cell proliferation

At Day 3, the cell proliferation in C scaffolds was significantly lower than in CS, CS@COL, and CS@TCP scaffolds. At Day 7, the cell proliferation in CS@COL and CS@TCP scaffolds remained significantly higher than that in C scaffolds. At Day 14, only the CS@TCP scaffolds showed a significant increase in proliferation compared to C scaffolds, as shown in Figure 4B. Live/dead staining results showed that cells exhibited better attachment on the CS@TCP and CS@COL scaffold surfaces compared to the C and CS scaffold surfaces, as shown in Figure 4C.

The morphologies of the coatings on Days 0 and 14 were similar, showing no obvious changes, while elemental analysis revealed a slight decrease in Ca content in the TCP-coated scaffolds (from 11.36 ± 0.39 wt.% to 11.10 ± 0.32 wt.%) and a more significant decrease in N content in the COL-coated scaffolds (from 17.81 ± 0.25 wt.% to 12.54 ± 0.36 wt.%), as shown in Figure 4D–G.

3.3. *In vitro* study of cell differentiation

The ALP staining, used to evaluate early osteogenic differentiation, revealed a markedly larger stained area in CS@TCP scaffolds compared to C, CS, and CS@COL

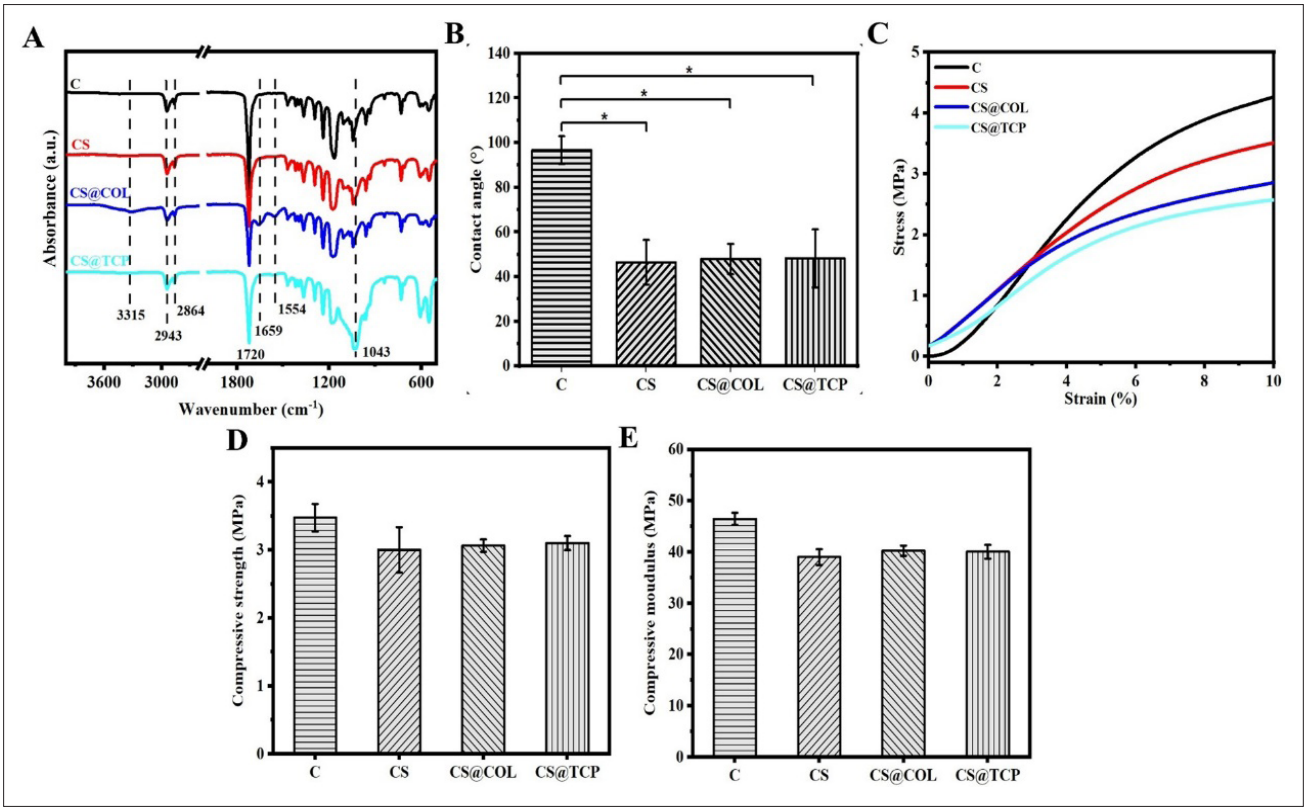

Figure 3. Physical and chemical characterizations for C, CS, CS@COL, and CS@TCP scaffolds. (A) Fourier transform infrared spectroscopy spectra. (B) Contact angle. (C) Stress–strain curves. (D) Compressive strength. (E) Compressive modulus. Notes: Data are expressed as mean ± SD; $n = 4$; *$p < 0.05$.

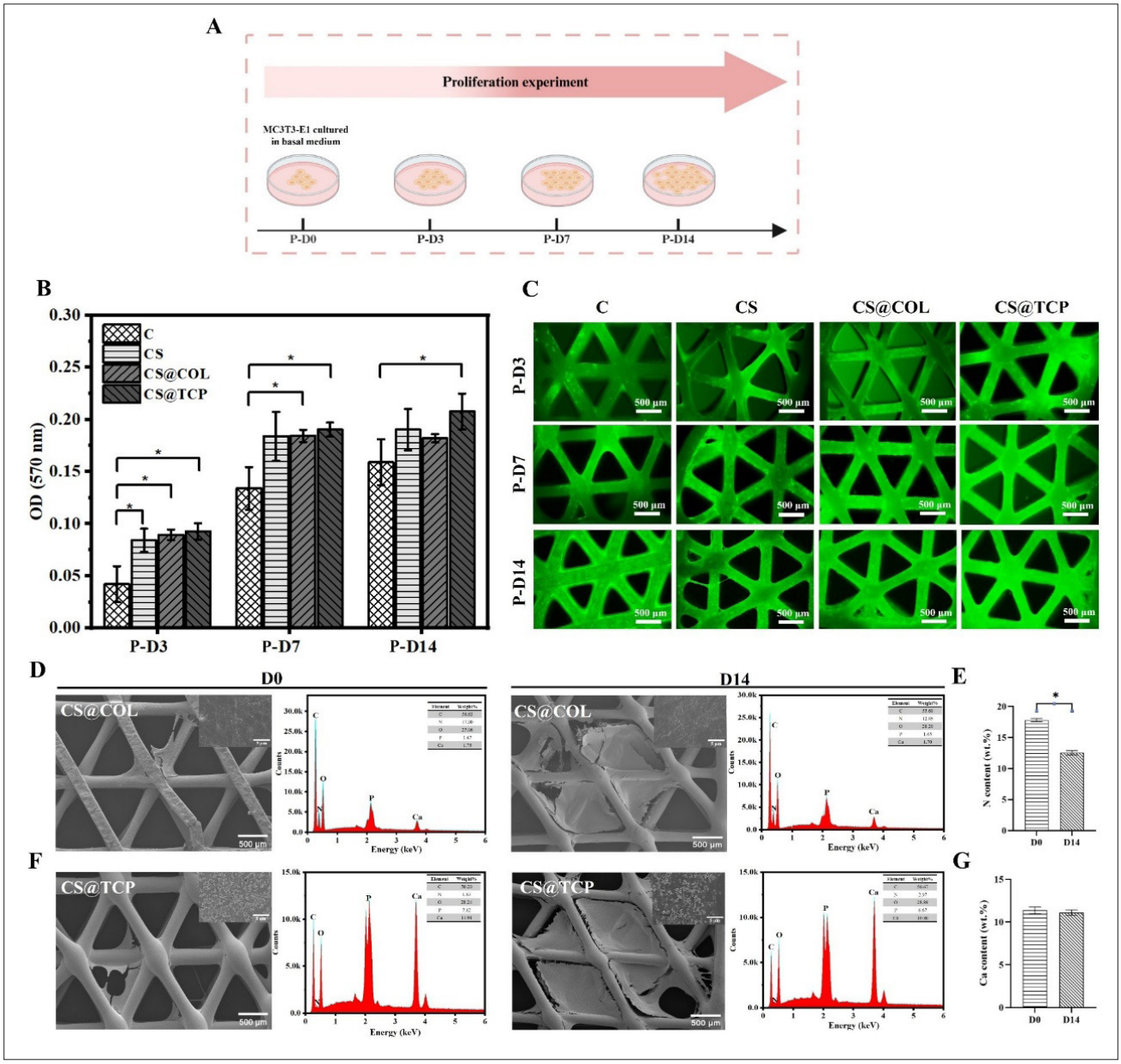

Figure 4. Cell proliferation studies for C, CS, CS@COL, and CS@TCP scaffolds. (A) Cell proliferation culture model. (B) MTT assay. (C) Live/dead staining. Scale bars: 500 μm; magnifications: ×5. (D–G) Scanning electron microscopy images (scale bars: 5 μm (insets); magnifications: ×100, ×10,000 (insets)); and energy dispersive X-ray spectroscopy mapping of scaffold coatings at Days 0 and 14 of cell culture: (D) CS@COL coatings and corresponding (E) N content; (F) CS@TCP coatings and corresponding (G) Ca content. Notes: Data are expressed as mean ± SD; $n = 4$; $^*p < 0.05$. Abbreviations: OD, optical density; P-D, proliferation day.

scaffolds, as illustrated in Figure 5B. At Days 14 and 21, the ALP activity in CS@TCP scaffolds was significantly higher than in C, CS, and CS@COL scaffolds, while CS scaffolds also showed significantly higher activity than C, as illustrated in Figure 5C. In contrast, ARS staining, which reflects late-stage mineral deposition, showed greater calcium deposition in CS@TCP scaffolds compared to the other groups, as shown in Figure 5D. ARS quantification further confirmed significantly higher mineral deposition in CS@TCP scaffolds relative to C and CS@COL groups at Days 14 and 21, as shown in Figure 5E.

3.4. *In vivo* micro-computed tomography evaluation

After 12 and 26 weeks of implantation, the Onlay group exhibited significantly lower values of BV/TV, BMD, and Tb.Th compared with the FTD and PTD groups, as

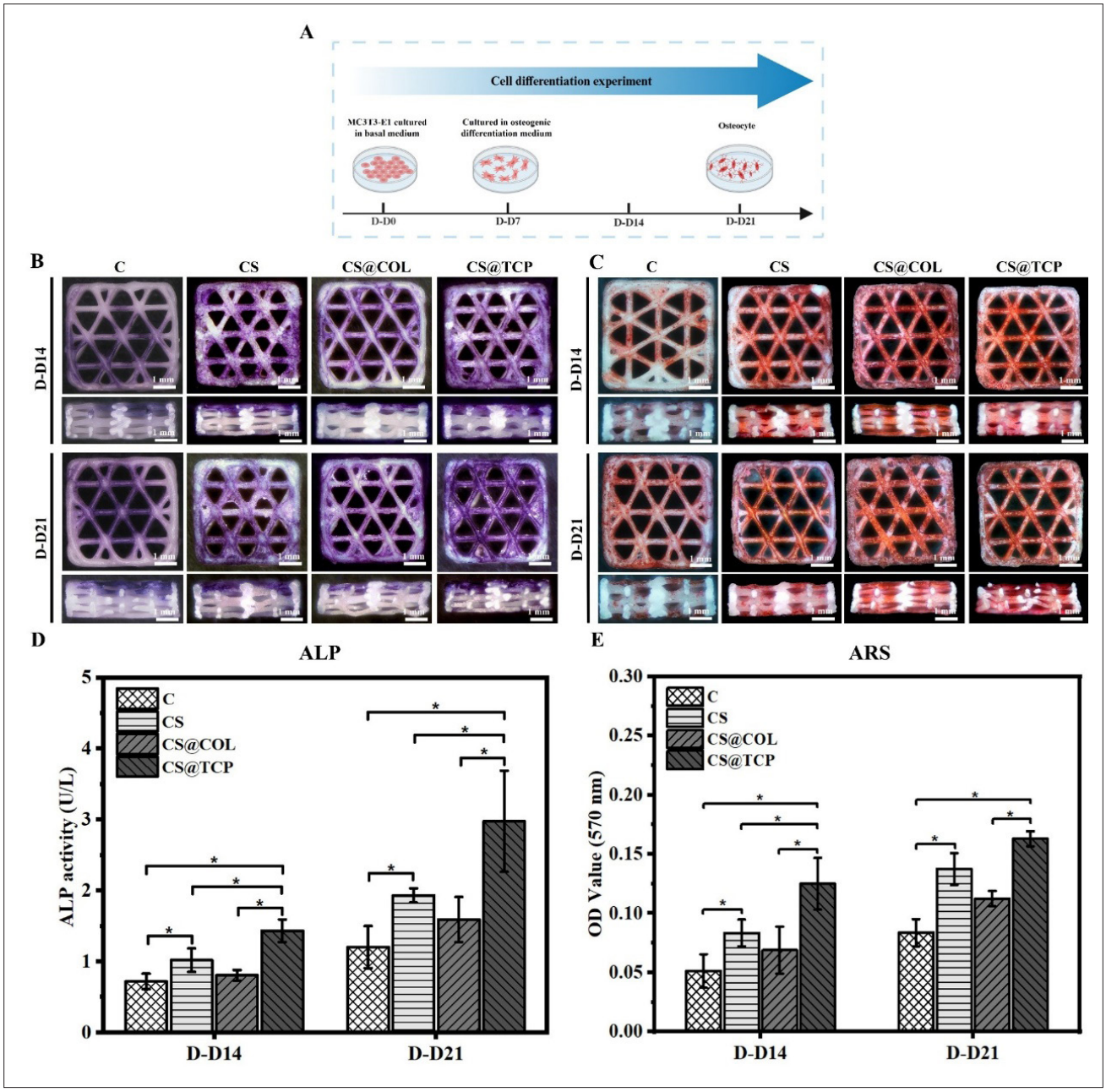

Figure 5. Cell differentiation studies for C, CS, CS@COL, and CS@TCP scaffolds. (A) Cell differentiation model. (B) Alkaline phosphatase (ALP)-stained images. Scale bars: 1 mm; magnifications: ×5. (C) Alizarin red S (ARS)-stained images. Scale bars: 1 mm; magnifications: ×5. (D) Quantitative analysis of ALP staining. (E) Quantitative analysis of ARS staining. Notes: Data are expressed as mean ± SD; $n = 4$; $^*p < 0.05$. Abbreviations: D-D, differentiation day; OD, optical density.

indicated in Figure 6C–F. Notably, the PTD group showed a significantly higher BV/TV than the FTD group at 12 weeks. In contrast, the Tb.N value in the Onlay group was significantly higher than that in the FTD and PTD groups at both 12 and 26 weeks, as shown in Figure 6F.

3.5. Histological analysis

The Onlay group consistently exhibited significantly lower osteoid levels compared to the FTD and PTD groups at 12 and 26 weeks, while the PTD group showed significantly lower osteoid formation than the FTD group at 26 weeks, as shown in Figure 7B. For mineralized bone formation,

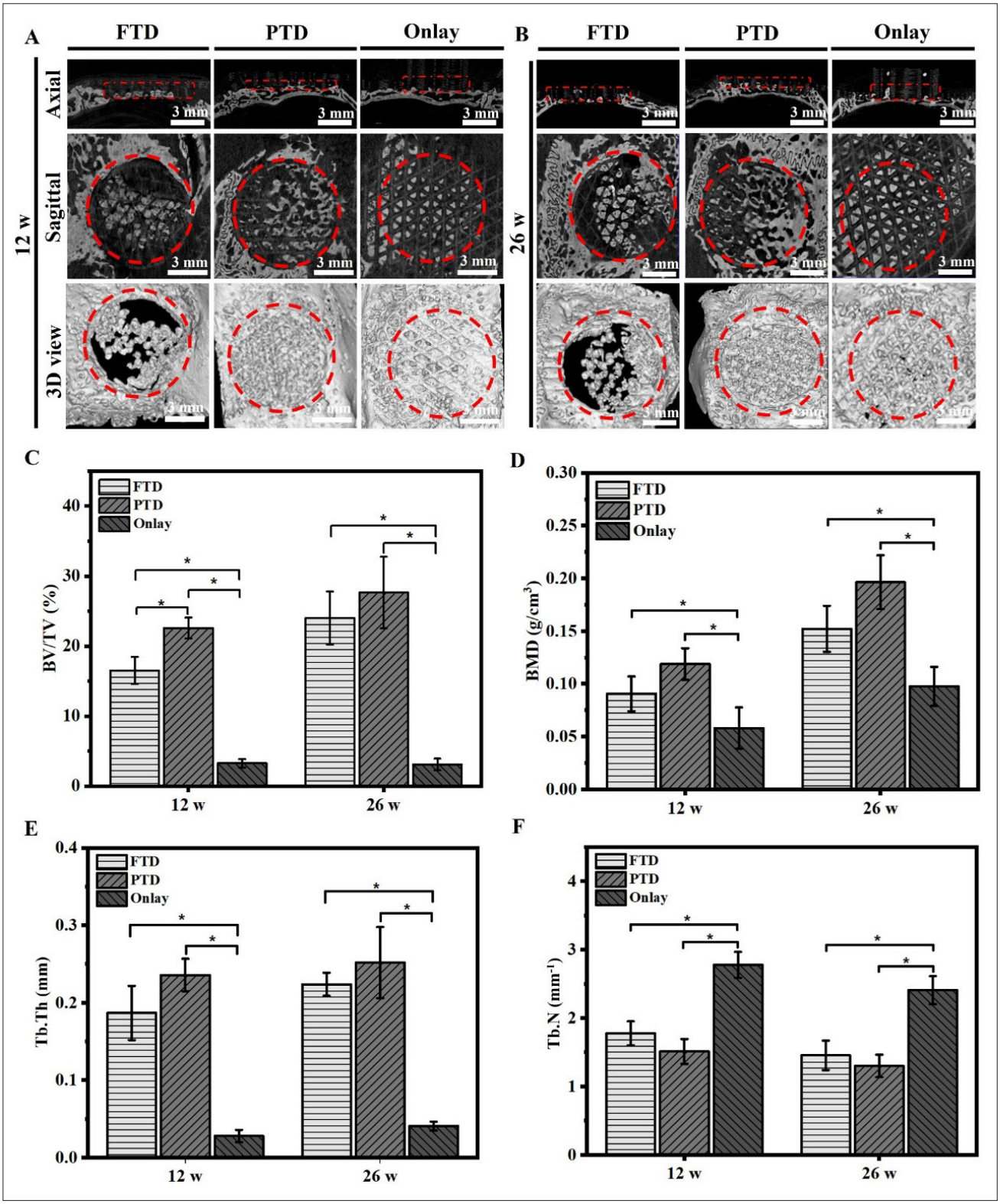

Figure 6. Micro-computed tomography (CT) evaluation of FTD, PTD, and Onlay groups after implantation for 12 and 26 weeks. Micro-CT axial, sagittal, and 3D reconstruction images at (A) 12 weeks and (B) 26 weeks. Scale bars: 3 mm; magnifications: ×1. (C) Bone volume/total volume (BV/TV). (D) Bone mineral density (BMD). (E) Trabecular thickness (Tb.Th). (F) Trabecular number (Tb.N). Notes: Data are expressed as mean ± SD; $n = 4$; $^*p < 0.05$. Abbreviations: FTD, full-thickness cranial defect; Onlay, intact cranial bone as an onlay graft; PTD, partial-thickness cranial defect.

the PTD group demonstrated significantly higher new bone formation than the FTD and Onlay groups at 26 weeks, while the Onlay group showed significantly lower new bone formation than the PTD and FTD groups at both 12 and 26 weeks, as illustrated in Figure 7C. Furthermore, collagen formation in the Onlay group was significantly lower than that in the FTD and PTD groups at both 12 and 26 weeks, as shown in Figure 7D.

3.6. Immunohistochemical analysis

In the PTD and FTD groups, the collagen staining intensity decreased from 12 to 26 weeks; in contrast, the Onlay group exhibited consistently higher collagen deposition compared to the other groups at both 12 and 26 weeks with limited variation, as shown in Figure 8B. A similar pattern was observed for vWF staining, which also declined from 12 to 26 weeks in the PTD and FTD groups. At 12 weeks, vWF staining intensity in the PTD group was significantly lower than that in the FTD group. Notably, the Onlay group consistently exhibited significantly greater vWF immunoreactivity than both the PTD and FTD groups at 12 and 26 weeks (Figure 8D).

4. Discussion

The success of bone tissue engineering primarily depends on the design of a supportive microenvironment, which integrates suitable scaffold architecture, surface chemistry, and bioactive modifications.[13–15] In this study, we developed 3D-printed PCL/β-TCP composite scaffolds

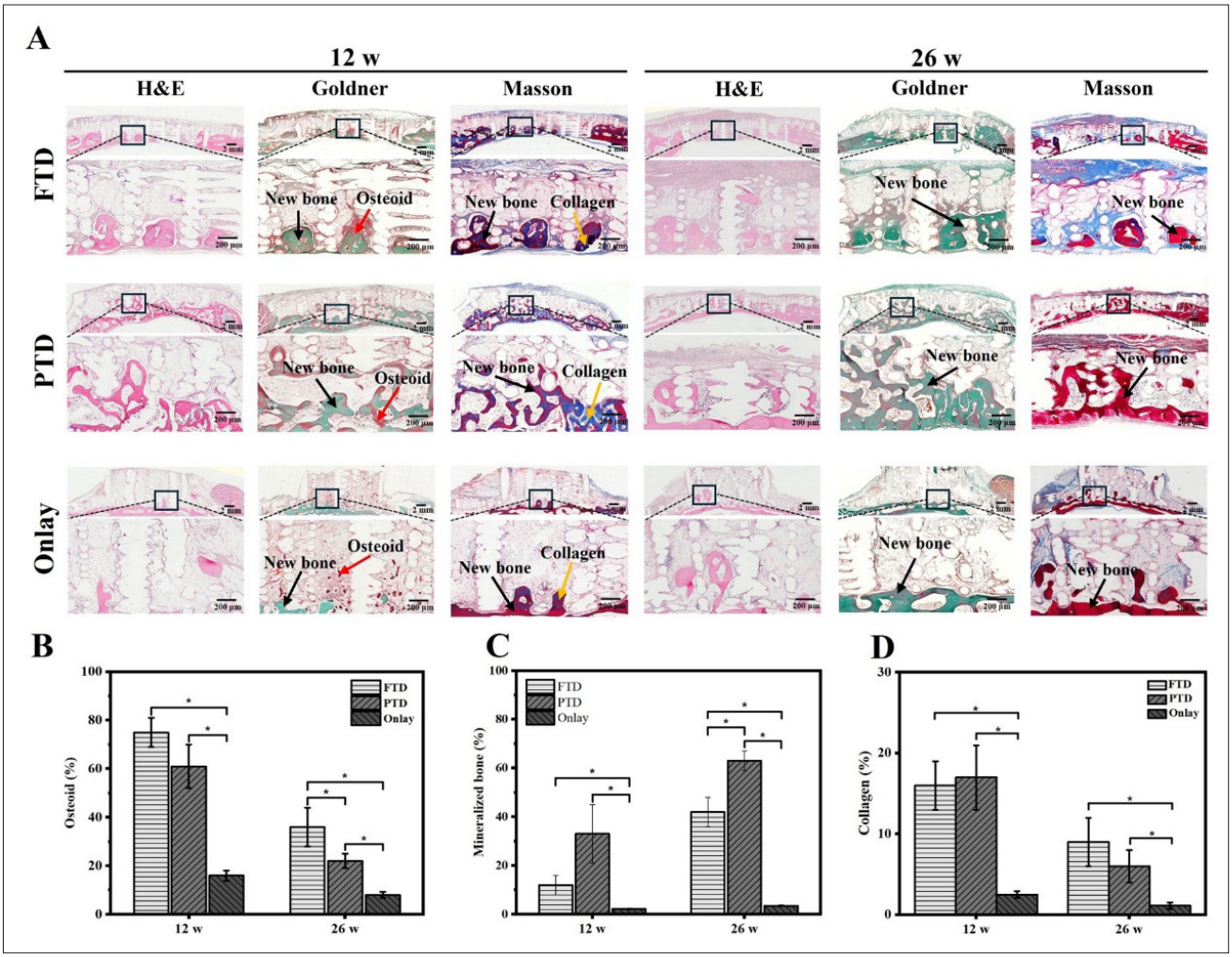

Figure 7. Histological analyses of FTD, PTD, and Onlay groups after implantation for 12 and 26 weeks. (A) Hematoxylin and eosin (H&E), Goldner's trichrome, and Masson's staining. Black arrows indicate new bone, red arrows indicate osteoid, and yellow arrows indicate collagen. Scale bars: 2 mm (top), 200 μm (bottom); magnifications: ×1 (top), ×4 (bottom). (B) Quantification of osteoid. (C) Quantification of mineralized bone. (D) Quantification of collagen. Notes: Data are expressed as mean ± SD; $n = 4$; *$p < 0.05$. Abbreviations: FTD, full-thickness cranial defect; Onlay, intact cranial bone as an onlay graft; PTD, partial-thickness cranial defect.

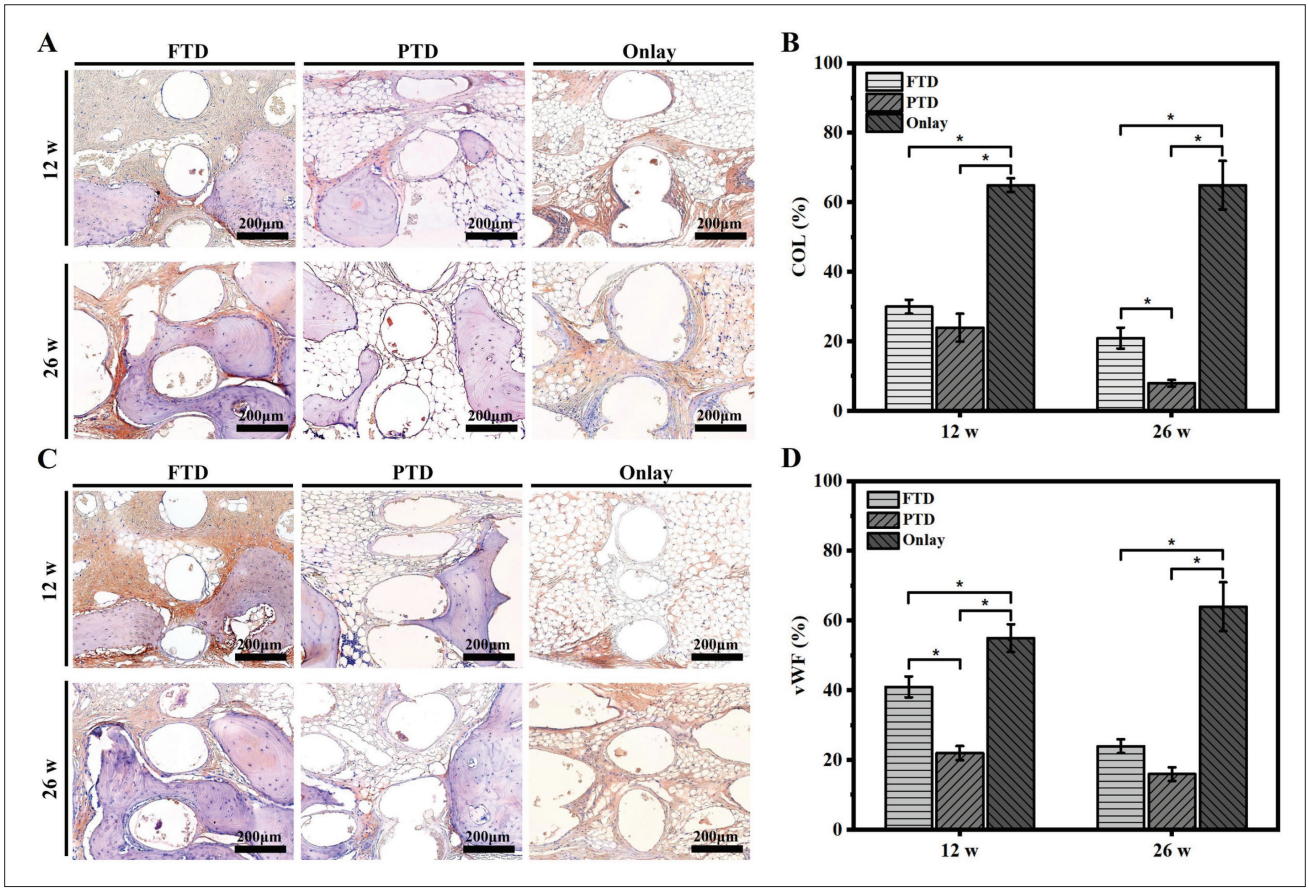

Figure 8. Immunohistochemical analyses of FTD, PTD, and Onlay groups after implantation for 12 and 26 weeks. (A) Collagen (COL)-stained images. Scale bars: 200 μm; magnifications: ×8. (B) Statistical analysis of COL expression. (C) Von Willebrand factor (vWF)-stained images. Scale bars: 200 μm; magnifications: ×8. (D) Statistical analysis of vWF expression. Notes: Data are expressed as mean ± SD; $n = 4$; $^*p < 0.05$. Abbreviations: FTD, full-thickness cranial defect; Onlay, intact cranial bone as an onlay graft; PTD, partial-thickness cranial defect.

with triangular-shaped pores. However, when applied as bone tissue engineering scaffolds, PCL/β-TCP composites still face challenges related to their hydrophobicity and low surface bioactivity.[16–18]

To address these issues, this study employed two different surface modification strategies using NaOH submersion followed by collagen and β-TCP coating, respectively.[19] NaOH modification proved highly effective in enhancing the hydrophilicity, protein adsorption, and cell adhesion properties of the scaffolds while maintaining their overall porous morphology.[20] In this study, a concentration of 2 M NaOH was used on PCL/β-TCP composite scaffolds, resulting in nanoscale pits on surfaces, accompanied by a significant decrease in contact angle. Notably, no obvious changes were detected in the EDS spectra, FTIR spectra, and mechanical properties after NaOH treatment, as illustrated in Figures 2 and 3.

Collagen, a major component of the extracellular matrix, has been widely used to enhance the bioactivity of tissue engineering scaffolds.[21] It has been demonstrated that collagen coating improves cell adhesion, proliferation, and osteogenic differentiation.[22,23] This phenomenon was attributed to the fact that extracellular matrix proteins provide a softer substrate for cell attachment, thereby promoting osteogenic gene expression.[24] β-TCP is a bioactive ceramic whose inorganic composition closely resembles that of natural bone and has been widely used in bone tissue engineering.[25,26] Moreover, β-TCP possesses excellent osteoconductive and osteoinductive properties that support cell attachment, proliferation, and differentiation.[27,28] Given these outstanding characteristics of collagen and β-TCP, the application of collagen and β-TCP has become a hot topic of research in bone graft coating materials.[29,30]

The 3D-printed PCL/β-TCP composite scaffolds were further surface-modified by depositing collagen and

β-TCP, leading to the formation of a collagen film and a nanoporous layer on the scaffold surface, as illustrated in Figure 2A. A notable increase in the N peak in CS@COL, and Ca and P peaks in CS@TCP scaffolds, along with the intensified FTIR bands at 3315, 1659, and 1,554 (amide A, I, and II for collagen), and 1043 cm^{-1} (β-TCP), further confirmed the successful coating of collagen and β-TCP on the scaffold surface, as shown in Figure 3A. Importantly, these surface modifications maintained their excellent hydrophilicity and mechanical properties, as demonstrated in Figure 3B–E.

Surface modification also plays an essential role in dictating cell behavior, as it creates a microenvironment that profoundly influences cell attachment, migration, proliferation, and differentiation.[31] Our *in vitro* results showed that cell proliferation was markedly enhanced in the CS, CS@COL, and CS@TCP scaffolds compared to the C scaffolds throughout the culture period, as illustrated in Figure 4. This may be attributed to the NaOH treatment, which improved the hydrophilicity and surface roughness of the scaffolds, thereby enhancing protein adsorption, facilitating cell attachment, and promoting cell proliferation.[32,33] In addition, our stability analysis revealed that the β-TCP coatings remained largely intact during the 14-day culture period, indicating greater stability compared to COL-coated scaffolds, as shown in Figure 4. For osteogenic differentiation, both ALP activity and ARS staining were significantly elevated in the CS@TCP group compared to the other groups, as shown in Figure 5D and E. It could be caused by the release of Ca^{2+} and PO_4^{3-} ions from β-TCP, which created an osteoinductive microenvironment and promoted early osteogenic activity. This effect may be mediated by stimulating osteogenic-related signaling pathways, such as Wnt/β-catenin and bone morphogenetic protein/Smad, thereby upregulating the expression of ALP, runt-related transcription factor 2, and osteocalcin.[34–38] For *in vivo* characterization, three different defect models were designed to systematically evaluate the osteogenic potential of the CS@TCP scaffolds. The FTD group simulated critical-sized bone defects to assess complete regenerative capability. Meanwhile, the PTD group allowed the investigation of scaffold–bone interface interactions, mimicking clinical inlay applications. The Onlay group mimicked the clinical application of cosmetic surgery, where implants were fixed on the bone surface.

In vivo results showed that both FTD and PTD groups exhibited significantly higher levels of new bone formation compared to the Onlay group, especially for the PTD group at 26 weeks, as presented in Figures 6 and 7. The expression of collagen and vWF in the Onlay group was consistently and significantly higher than that in other groups at both time points. Additionally, the FTD group showed a higher collagen and vWF expression compared to the PTD group, as shown in Figure 8. This may be due to the β-TCP coating on the scaffold surface. When in direct contact with the periosteum, the coating can enhance the recruitment of mesenchymal stem cells (MSCs), promoting efficient graft–host bone integration.[39] The decreasing trend in collagen and vWF expression over time in FTD and PTD groups likely reflects the tissue remodeling process during bone healing.[40] In contrast, the persistently higher expression of collagen and vWF in the Onlay group compared to the other groups at 12 and 26 weeks may reflect the early osteogenic stage rather than active osteogenesis, as shown in Figure 8.[41,42]

The overall reasons for these phenomena are illustrated in Figure 9. In the PTD group, the scaffolds were implanted within partial bone defects, where increased vascular supply and endogenous stem cells could enhance graft–host integration and induce higher levels of new bone formation.[43] This process synergistically interacted with the β-TCP coating on the scaffold surface, promoting MSC recruitment, osteogenic differentiation, and bone regeneration. In contrast, the coating in the FTD group had less contact with the host bone compared to the PTD group, restricting its new bone ingrowth.[44] Furthermore, in the Onlay group, where the scaffold was placed on the periosteum without direct exposure to MSCs or injury-related stimuli, the regenerative microenvironment was less supportive, resulting in limited bone integration only near the graft–bone surfaces.[42,45] Nonetheless, these bone integration effects can still facilitate the major goal of cosmetic surgeries.

In summary, these results highlighted the necessity of aligning scaffold design and surface biofunctionalization with specific clinical contexts to achieve optimal bone regeneration outcomes. Future work should further investigate the interaction between scaffolds and immune/vascular systems, thereby providing a deeper insight into the signaling pathways that regulate osteogenic and angiogenic properties *in vitro* and *in vivo*.

5. Conclusion

Scaffolds for bone tissue engineering aim to restore bone defects through the integration of biomaterials and regenerative microenvironments. This study demonstrated that integrating bioactive coatings with NaOH-pretreated 3D-printed PCL/β-TCP scaffolds effectively enhances scaffold hydrophilicity and bioactivity without compromising compressive properties. The β-TCP coating significantly promoted early osteogenic differentiation *in vitro*, potentially through ion release-mediated stimulation of osteoblast activity. The *in vivo* regenerative outcome

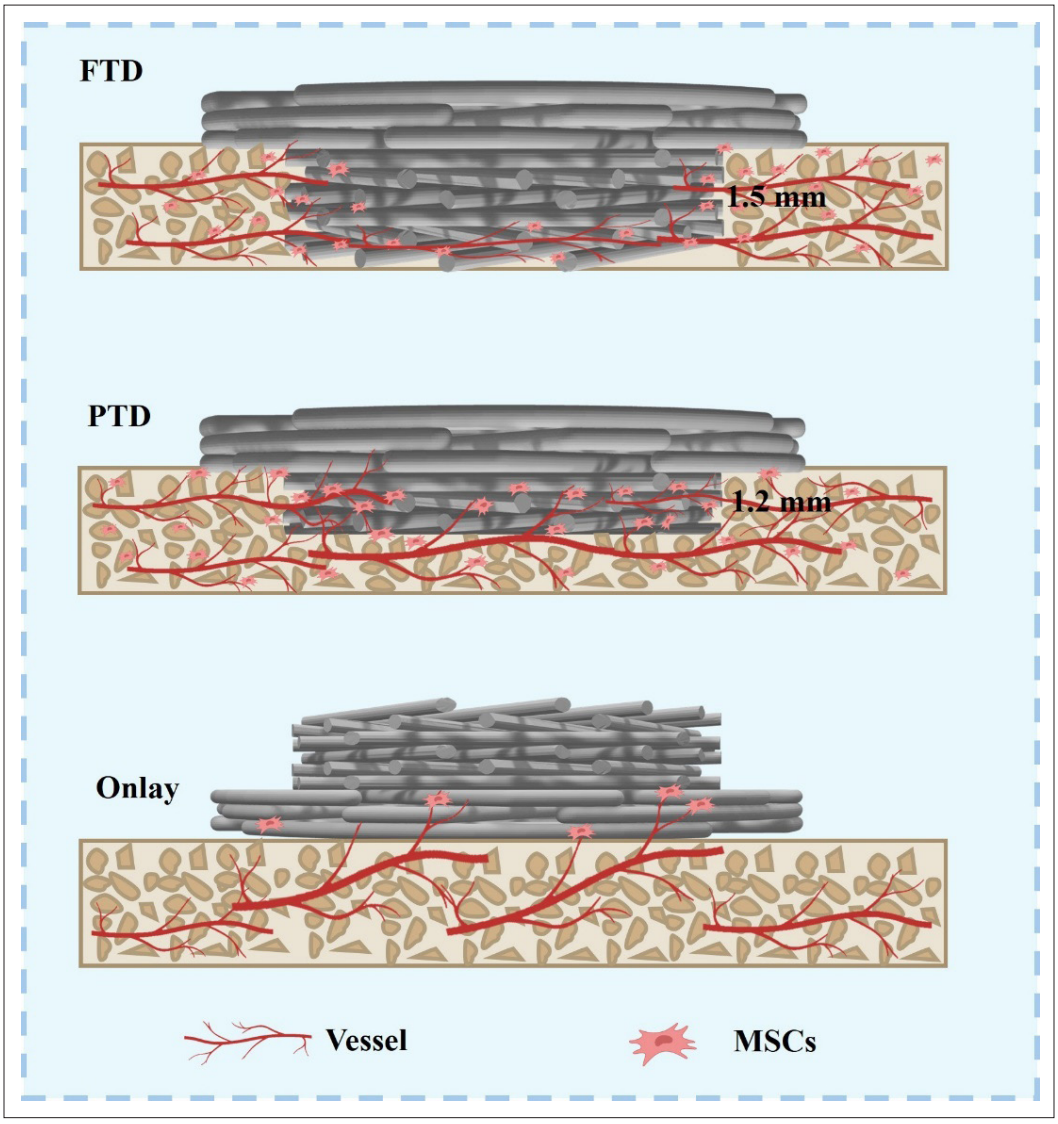

Figure 9. Schematic illustration of three cranial defect models (FTD, PTD, and Onlay) showing differences in scaffold placement and bone repair mechanism. Abbreviations: FTD, full-thickness cranial defect; MSC, mesenchymal stem cell; Onlay, intact cranial bone as an onlay graft; PTD, partial-thickness cranial defect.

was strongly influenced by the microenvironment. The PTD group provided abundant vascular supply and endogenous stem cells, enabling a synergistic interaction with the β-TCP coating and resulting in the highest level of new bone formation. The Onlay group showed new bone formation primarily at the scaffold–host bone interface, which could achieve the goal of excellent bone integration during the application of cosmetic surgeries. Collectively, these findings highlight the importance of tailoring scaffold structure and surface functionalization strategies to specific clinical scenarios, thereby maximizing bone regeneration and facilitating the reliable clinical application of 3D-printed bone scaffolds.

Acknowledgments

None.

Funding

The study was funded by the Natural Science Foundation of Jiangsu Province (BK20210117).

Conflict of interest

Yulin Jiang, Guanghui Xi, Chen Zhou, Xi Yang, and Dongxu Ke are employees of Novaprint Therapeutics

Suzhou Co., Ltd during this study but had no involvement in activities posing a conflict of interest.
The authors declare that they have no known competing financial interests or personal relationships that could have appeared to influence the work reported in this paper.

Author contributions

Conceptualization: Dongxu Ke, Yulin Jiang, Haisong Xu, Xi Yang
Investigation: Yulin Jiang, Guanghui Xi, Haisong Xu
Methodology: Yulin Jiang, Guanghui Xi, Haisong Xu, Chen Zhou
Software: Chen Zhou, Xi Yang
Writing–original draft: Yulin Jiang, Guanghui Xi
Writing–review & editing: Dongxu Ke, Yulin Jiang, Guanghui Xi, Xi Yang, Haisong Xu

Ethics approval and consent to participate

All procedures followed the NIH Guide for the Care and Use of Laboratory Animals and were approved by the Shanghai Jiao Tong University Agricultural Experimental Animal Farm (JDLL-R-20231016).

Consent for publication

Not applicable.

Availability of data

All data that support the findings of this study are included within the article.

References

1. Yelin E, Weinstein S, King T. The burden of musculoskeletal diseases in the United States. *Semin Arthritis Rheum*. 2016;46(3):259-260. doi:10.1016/j.semarthrit.2016.07.013
2. Ong KL, Mowat FS, Chan N, *et al*. Economic burden of revision hip and knee arthroplasty in Medicare enrollees. *Clin Orthop Relat Res*. 2006;446:22-28. doi:10.1097/01.blo.0000214439.95268.59
3. Huang D, Li Z, Li G, *et al*. Biomimetic structural design in 3D-printed scaffolds for bone tissue engineering. *Mater Today Bio*. 2025;32:101664. doi:10.1016/j.mtbio.2025.101664
4. Tsiklin IL, Shabunin AV, Kolsanov AV, Volova LT. In vivo bone tissue engineering strategies: advances and prospects. *Polymers (Basel)*. 2022;14(15):3222. doi:10.3390/polym14153222
5. Wu Y, Ji Y, Lyu Z. 3D printing technology and its combination with nanotechnology in bone tissue engineering. *Biomed Eng Lett*. 2024;14(3):451-464. doi:10.1007/s13534-024-00350-x
6. Wen Y, Xun S, Haoye M, *et al*. 3D printed porous ceramic scaffolds for bone tissue engineering: a review. *Biomater Sci*. 2017;5(9):1690-1698. doi:10.1039/c7bm00315c
7. Meng F, Yin Z, Ren X, Geng Z, Su J. Construction of local drug delivery system on titanium-based implants to improve osseointegration. *Pharmaceutics*. 2022;14(5):1069. doi:10.3390/pharmaceutics14051069
8. Sun S, Liu H, Hu Y, *et al*. Selection and identification of a novel ssDNA aptamer targeting human skeletal muscle. *Bioact Mater*. 2023;20:166-178. doi:10.1016/j.bioactmat.2022.05.016
9. Wang Q, Ye W, Ma Z, *et al*. 3D printed PCL/β-TCP cross-scale scaffold with high-precision fiber for providing cell growth and forming bones in the pores. *Mater Sci Eng C Mater Biol Appl*. 2021;127:112197. doi:10.1016/j.msec.2021.112197
10. Weingärtner L, Latorre SH, Velten D, *et al*. The effect of collagen-I coatings of 3D printed PCL scaffolds for bone replacement on three different cell types. *Appl Sci*. 2021;11(22):11063. doi:10.3390/app112211063
11. Jiang Y, Zhou C, Yang X, Ke D. 3D printed bioactive coated scaffolds boost osteogenesis and angiogenesis via the regulation of scaffold microstructure. *Biofabrication*. 2025;17(3):1-18. doi:10.1088/1758-5090/addc9c
12. Furtado ASA, Cunha MHS, Sousa LMR, *et al*. 3D-printed PCL-based scaffolds with high nanosized synthetic smectic clay content: fabrication, mechanical properties, and biological evaluation for bone tissue engineering. *Int J Nanomedicine*. 2025;20:53-69. doi:10.2147/IJN.S497539
13. Hao S, Wang M, Yin Z, *et al*. Microenvironment-targeted strategy steers advanced bone regeneration. *Materials Today Bio*. 2023;22:100741. doi:10.1016/j.mtbio.2023.100741
14. Zhu G, Zhang T, Chen M, *et al*. Bone physiological microenvironment and healing mechanism: basis for future bone-tissue engineering scaffolds. *Bioact Mater*. 2021;6(11):4110-4140. doi:10.1016/j.bioactmat.2021.03.043
15. Koushik TM, Miller CM, Antunes E. Bone tissue engineering scaffolds: function of multi-material hierarchically structured scaffolds. *Adv Healthc Mater*. 2023;12(9):2202766. doi:10.1002/adhm.202202766
16. Riau AK, Venkatraman SS, Mehta JS. Biomimetic vs. direct approach to deposit hydroxyapatite on the surface of low melting point polymers for tissue engineering. *Nanomaterials*. 2020;10(11):2162. doi:10.3390/nano10112162

17. Shen HY, Xing F, Shang SY, *et al*. Biomimetic mineralized 3D-printed polycaprolactone scaffold induced by self-adaptive nanotopology to accelerate bone regeneration. *ACS Appl Mater Interfaces*. 2024;16(15):18658-18670. doi:10.1021/acsami.4c02636

18. Heo SY, Ko SC, Oh GW, *et al*. Fabrication and characterization of the 3D-printed polycaprolactone/fish bone extract scaffolds for bone tissue regeneration. *J Biomed Mater Res B Appl Biomater*. 2019;107(6):1937-1944. doi:10.1002/jbm.b.34286

19. Tawfick S, De Volder M, Copic D, *et al*. Engineering of micro- and nanostructured surfaces with anisotropic geometries and properties. *Adv Mater*. 2012;24(13): 1628-1674. doi:10.1002/adma.201103796

20. Kocagöz M, Tıhmınlıoğlu F, Aldemir Dikici B. Surface modification *via* alkali treatment and its effect on the physicochemical and biological properties of emulsion templated scaffolds. *Polymer*. 2025;330:128475. doi:10.1016/j.polymer.2025.128475

21. Sherman VR, Yang W, Meyers MA. The materials science of collagen. *J Mech Behav Biomed Mater*. 2015;52:22-50. doi:10.1016/j.jmbbm.2015.05.023

22. Gresita A, Raja I, Petcu E, Hadjiargyrou M. Collagen-coated hyperelastic bone promotes osteoblast adhesion and proliferation. *Materials (Basel)*. 2023;16(21):6996. doi:10.3390/ma16216996

23. Vandrovcová M, Douglas T, Hauk D, *et al*. Influence of collagen and chondroitin sulfate (CS) coatings on poly-(lactide-co-glycolide) (PLGA) on MG 63 osteoblast-like cells. *Physiol Res*. 2011;60(5):797-813. doi:10.33549/physiolres.931994

24. Valdoz JC, Johnson BC, Jacobs DJ, *et al*. The ECM: to scaffold, or not to scaffold, that is the question. *Int J Mol Sci*. 2021;22(23):12690. doi:10.3390/ijms222312690

25. Jeong J, Kim JH, Shim JH, Hwang NS, Heo CY. Bioactive calcium phosphate materials and applications in bone regeneration. *Biomater Res*. 2019;23:4. doi:10.1186/s40824-018-0149-3

26. Boda R, Lázár I, Keczánné-Üveges A, *et al*. β-Tricalcium phosphate-modified aerogel containing PVA/Chitosan hybrid nanospun scaffolds for bone regeneration. *Int J Mol Sci*. 2023;24(8):7562. doi:10.3390/ijms24087562

27. Silva-Barroso AS, Cabral CSD, Ferreira P, Moreira AF, Correia IJ. Lignin-enriched tricalcium phosphate/sodium alginate 3D scaffolds for application in bone tissue regeneration. *Int J Biol Macromol*. 2023;239:124258. doi:10.1016/j.ijbiomac.2023.124258

28. Lu Q, Diao J, Wang Y, *et al*. 3D printed pore morphology mediates bone marrow stem cell behaviors via RhoA/ROCK2 signaling pathway for accelerating bone regeneration. *Bioact Mater*. 2023;26:413-424. doi:10.1016/j.bioactmat.2023.02.025

29. Zheng J, Nozaki K, Hashimoto K, Yamashita K, Wakabayashi N. Exploring the biological impact of β-TCP surface polarization on osteoblast and osteoclast activity. *Int J Mol Sci*. 2024;26(1):141. doi:10.3390/ijms26010141

30. Lu J, Yu H, Chen C. Biological properties of calcium phosphate biomaterials for bone repair: a review. *RSC Adv*. 2018;8(4):2015-2033. doi:10.1039/c7ra11278e

31. Deng W, Yang X, Yu J, Omari-Siaw E, Xu X. Recent advances of physiochemical cues on surfaces for directing cell fates. *Colloids Surf B Biointerfaces*. 2025;250:114550. doi:10.1016/j.colsurfb.2025.114550

32. Gupta D, Singh AK, Kar N, Dravid A, Bellare J. Modelling and optimization of NaOH-etched 3-D printed PCL for enhanced cellular attachment and growth with minimal loss of mechanical strength. *Mater Sci Eng C*. 2019;98:602-611. doi:10.1016/j.msec.2018.12.084

33. Jiang L, Jin S, Geng S, *et al*. Maintenance and restoration effect of the surface hydrophilicity of pure titanium by sodium hydroxide treatment and its effect on the bioactivity of osteoblasts. *Coatings*. 2019;9(4):222. doi:10.3390/coatings9040222

34. Witek L, Shi Y, Smay J. Controlling calcium and phosphate ion release of 3D printed bioactive ceramic scaffolds: an in vitro study. *J Adv Ceram*. 2017;6(2):157-164. doi:10.1007/s40145-017-0228-2

35. Luo F, Yang Y, Li D, *et al*. Low-temperature plasma effect-induced enhancement of osteogenic activity in calcium phosphate ceramics. *Acta Biomater*. 2025;200:667-685. doi:10.1016/j.actbio.2025.04.048

36. González Díaz EC, Shih YRV, Nakasaki M, Liu M, Varghese S. Mineralized biomaterials mediated repair of bone defects through endogenous cells. *Tissue Eng Part A*. 2018;24(13–14):1148-1156. doi:10.1089/ten.tea.2017.0297

37. Weng Y, Jian Y, Huang W, *et al*. Alkaline earth metals for osteogenic scaffolds: from mechanisms to applications. *J Biomed Mater Res B Appl Biomater*. 2023;111(7):1447-1474. doi:10.1002/jbm.b.35246

38. Wang K, Jiang K, Luo C, *et al*. An osteoimmunomodulatory Ca2+/Zn2+-doped scaffold promotes M2 macrophage polarization via the src-mediated chemoking signaling pathway to enhance osteoinduction. *Compos Part B: Eng*. 2024;284:111653. doi:10.1016/j.compositesb.2024.111653

39. Ghiacci G, Graiani G, Ravanetti F, *et al*. "Over-inlay" block graft and differential morphometry: a novel block graft model to study bone regeneration and host-to-graft interfaces in

rats. *J Periodontal Implant Sci*. 2016;46(4):220-233. doi:10.5051/jpis.2016.46.4.220

40. Selvaraj V, Sekaran S, Dhanasekaran A, Warrier S. Type 1 collagen: synthesis, structure and key functions in bone mineralization. *Differentiation*. 2024;136:100757. doi:10.1016/j.diff.2024.100757

41. Pilliar RM, Lee JM, Maniatopoulos C. Observations on the effect of movement on bone ingrowth into porous-surfaced implants. *Clin Orthop Relat Res*. 1986;7(208):108-113.

42. Sosakul T, Tuchpramuk P, Suvannapruk W, *et al*. Evaluation of tissue ingrowth and reaction of a porous polyethylene block as an onlay bone graft in rabbit posterior mandible. *J Periodontal Implant Sci*. 2020;50(2):106-120. doi:10.5051/jpis.2020.50.2.106

43. Canto FRT, Garcia SB, Issa JPM, *et al*. Influence of decortication of the recipient graft bed on graft integration and tissue neoformation in the graft-recipient bed interface. *Eur Spine J*. 2008;17(5):706-714. doi:10.1007/s00586-008-0642-9

44. Wu S, Luo S, Cen Z, *et al*. All-in-one porous membrane enables full protection in guided bone regeneration. *Nat Commun*. 2024;15(1):119. doi:10.1038/s41467-023-43476-9

45. Ku JK, Lee KG, Ghim MS, *et al*. Onlay-graft of 3D printed Kagome-structure PCL scaffold incorporated with rhBMP-2 based on hyaluronic acid hydrogel. *Biomed Mater*. 2021;16(5):055004. doi:10.1088/1748-605X/ac0f47